The DOI for this manuscript is doi: 10.1175/JHM-D-12-0189.1

Atmospheric Rivers and Extreme Cool Season Precipitation Events in the Verde River Basin of Arizona

Erick R. Rivera[1], Francina Dominguez[*1,2] and Christopher L. Castro[1]

[1] Department of Atmospheric Sciences, The University of Arizona, Tucson, Arizona.

[2] Department of Hydrology and Water Resources, The University of Arizona, Tucson, Arizona.

[*]Corresponding author address: Department of Atmospheric Sciences, University of Arizona, PAS 81, Room 542, 1118 E 4th St, PO Box 210081, Tucson, AZ 85721-0081. Email: francina@hwr.arizona.edu.

Abstract

Inland-penetrating atmospheric rivers (ARs) can affect the Southwestern United States (US) and significantly contribute to cool season (November to March) precipitation. In this work, a climatological characterization of AR events that have led to extreme cool season precipitation in the Verde River Basin (VRB) in Arizona for the period 1979/80-2010/11 is presented. A "bottom-up" approach is used by first evaluating extreme daily precipitation in the basin associated with AR occurrence, then identifying the two dominant AR patterns (referred to as Type 1 and Type 2, respectively) using a combined EOF statistical analysis. The results suggest that Southwestern AR events do not form and develop in the same regions. Water vapor content in Type 1 ARs is obtained from the tropics near Hawaii (central Pacific) and enhanced in the midlatitudes, with maximum moisture transport over ocean at low-levels of the troposphere. On the other hand, moisture in Type 2 ARs has a more direct tropical origin and meridional orientation with maximum moisture transfer at mid-levels. Nonetheless, both types of ARs cross the Baja Peninsula before affecting the VRB. In addition to Type 1 and Type 2 ARs, observations reveal AR events that are a mixture of both patterns. These cases can have water vapor transport patterns with both zonal and meridional signatures, and they can also present double peaks in moisture transport at low-levels and mid-levels. This seems to indicate that the two "types" can be interpreted as end points of a range of possible directions.

1. Introduction

Atmospheric rivers (ARs) are filamentary water vapor fluxes that cover about 10% of the globe and are responsible for most of the meridional water vapor transport in the extratropical atmosphere (Zhu and Newell 1998). These features are typically located in the warm sector of major extratropical cyclones where a pre-cold front low-level jet (LLJ) is present (Ralph et al. 2004, 2005, 2006; Neiman et al. 2008; Dettinger et al. 2011; Ralph and Dettinger 2011). Generally, ARs are 400-600 km wide and thousands of kilometers long (Ralph et al. 2004; Ralph and Dettinger 2012). They show integrated water vapor (IWV) amounts above 2 cm and most of the associated water vapor transport occurs in the lowest 2.5 km of the atmosphere (Ralph et al. 2005; Neiman et al. 2008).

ARs are typically identified using IWV or integrated water vapor transport (IWVT), however, integration in the vertical removes the three-dimensional nature of ARs and their interrelation with synoptic-scale forcing (Sodemann and Stohl, 2013). This is particularly important for the Southwestern US because, in contrast to the midlatitudes, subtropical poleward moisture transport in the North Pacific will generally occur at mid-levels, and above the planetary boundary layer (Knippertz and Martin, 2007). Previous studies have made a distinction between mid-level moisture transport and ARs, and assigned the term "moisture conveyor belt" (MCB) to enhanced water vapor transport at around 700 hPa that occurs in association with quasi-stationary upper level cut-off lows (Knippertz and Martin, 2007). In our study we use the term AR for all events occurring in narrow bands with enhanced IWVT that satisfy the criteria of Zhu and Newell (1998) and Ralph et al. (2012), without differentiating between low-level and mid-level transport (much like Stohl et al. 2008). The simplicity of using a unified perspective is useful when analyzing extreme events that are of interest to other communities such as hydrologists (Sodemann and Stohl, 2013).

Due to the complex topography in the West Coast of the United States (US) and the proximity to water vapor sources from the Pacific Ocean, orographically-enhanced cold season extreme precipitation events and seasonal snow accumulations have been extensively related to the occurrence of landfalling ARs (Leung and Qian 2009; Smith et al. 2010; Dettinger et al. 2011; Ralph et al. 2011). Currently, IWV fields either from composite daily Special Sensor Microwave Imager (SSM/I) (Hollinger et al. 1990) satellite retrievals or atmospheric models are analyzed using objective and automated tools in order to detect ARs (e.g., Wick et al. 2013). SSM/I measurements indicate that the wintertime ARs affecting the western coast of North America extend northeastward from the tropical Pacific Ocean. The ARs with the largest IWV (> 3 cm) are typically associated with stronger storms and higher precipitation accumulations (Neiman et al. 2008).

As an example, Ralph et al. (2006) used meteorological measurements from field campaigns and IWV observations from the SSM/I to establish a connection between a landfalling AR and the flooding that occurred in the Russian River in February 2004. During this event, more than 250 mm of rain in a 2.5-day period was registered in the coastal mountains of northern California. In fact, their study reveals that all of the seven floods in the Russian River between October 1997 and December 2005 were related to AR episodes. More recently, a succession of strong ARs produced between 250 and 670 mm of rain in mountainous areas extending from Washington to California during a 14-day period in December 2010 (Ralph and Dettinger 2012). That series of ARs were responsible for heavy rain and flooding and substantially increased snowpack in the region. Guan et al. (2010) analyzed in situ, remotely-sensed and assimilated data for the water years 2004–2010 and concluded that wintertime ARs contribute to approximately 30-40% of the total annual snow water equivalent accumulations in the Sierra Nevada. Additionally, Dettinger et al. (2011) determined that, on long-term average, about 20-50% of the annual precipitation in California is produced by ARs. They also found similar contributions to the overall streamflow.

Although most of the research on ARs has addressed the importance of these phenomena in the generation of precipitation extremes and flooding events in regions such as the western coasts of the continents (e.g., Ralph et al. 2006; Neiman et al. 2008; 2011; Stohl et al. 2008; Roberge et al. 2009; Viale and Nuñez 2011; Lavers et al. 2012, Lavers and Villarini 2013), little is known to date about the effects of the ARs that penetrate further inland. Knippertz and Martin (2007) studied the influence of a mid-level cut-off low in the generation of elongated poleward water vapor flux from the tropics (MCB), which produced a heavy precipitation event in the Southwestern US during November 2003. The work by Dettinger et al. (2011) shows that the contribution of ARs to the total cool season precipitation in the Southwest, particularly in several portions of Arizona and New Mexico, during the water years 1998–2008 is approximately less than 10%. However, their analysis only took into account the ARs that made landfall between 32.5° N (international US - Mexico border) and 52.5°N. In a following study, Rutz and Steenburgh (2012) argue that this percentage is underestimated because the contribution of ARs intersecting the west coast of the Baja Peninsula in Mexico (between 24° N and 32.5° N) was not considered. These authors showed that the fraction of AR-related cool season precipitation increases by more than 15% in some areas of southern California, Nevada and Arizona when extending the analysis of landfalling ARs southward from 32.5° N. More recently, Neiman et al. (2013) provided a very detailed description of a series of ARs that produced very heavy precipitation and flooding in Arizona's Mogollon Rim during late January of 2010 using an array of observations and gridded datasets. Their results show that these events are comparable to the typical West Coast ARs. Moore et al. (2012) also found a connection between an AR episode and a major flooding event in the Southeastern US in May 2010.

The analysis of ARs is particularly important in the semiarid Southwestern US because this region is dependent on winter precipitation for its water resources. Despite the fact that peak precipitation in the Southwest occurs during the summer monsoon season, this precipitation is significantly depleted due to high evapotranspiration rates. On the other hand, cool season precipitation is generally stored as snow and released slowly in the warmer part of the year as surface runoff or infiltration. The most important moisture source of winter precipitation in the Southwestern US is the westerly storm tracks that form over the Pacific Ocean (Redmond and Koch 1991; Adams and Comrie 1997; Sheppard et al. 2002). When these tracks shift southward, the region may experience periods of more intense rains (e.g., Sheppard et al. 2002; Cavazos and Rivas 2004). In addition, some inland watersheds, such as the Verde and Salt River basins in central Arizona, are located in regions in which moisture transported from the Pacific Ocean can interact with local mountain barriers to produce orographic precipitation. In the historical records, we find that some cool season extreme precipitation events have severely impacted the region. In January and February 1993, a very active storm season led to the occurrence of heavy flooding events in portions of Arizona (House and Hirschboeck 1997) which resulted in human casualties and injuries as well as damages in excess of US$400 million (US Army Corps of Engineers 1994). The intense storms of 11-13 February 2005 caused US$6.5 million in damage in the Phoenix area (The Flood Control District of Maricopa County, http://www.fcd.maricopa.gov/education/history.aspx). As we will show in this work, both of these events are characteristic AR-related floods in the region.

In this work we provide the first climatological characterization of ARs that bring oceanic moisture to the Southwestern US during the cool season. In particular, we explore the connection between ARs and extreme precipitation in the Verde River Basin (VRB) (see Figure 1) in central Arizona. The VRB is a relatively large watershed of about 14,115 km^2 that encompasses part of the Coconino Plateau in its northern portion, with the Mogollon Rim defining its eastern boundary (http://www.azwater.gov). Water supply to the city of Phoenix relies on allocations from the Colorado River, as well as deliveries from the Salt and Verde River basins. For this reason, it is important to understand how ARs can affect extreme cool season precipitation in these inland watersheds.

Similarly to Neiman et al. (2011), our work has a "bottom-up" approach, as we first identify extreme precipitation events in the VRB and then evaluate the atmospheric conditions that lead to these extreme episodes in order to determine any connection with AR occurrence. Then, we perform both statistical and composite analyses to characterize the dominant spatial patterns associated with the impacting ARs in the region and compare them with the better-known US West Coast ARs.

This paper is organized as follows: a description of the data and the methodology is provided in Section 2. In Section 3 we present the results of the AR identification method, the regional hydrological impacts of the impacting ARs as well as the statistical and composite analyses to characterize the dominant atmospheric patterns related to AR occurrence. Additionally, we examine two intense AR events that produced heavy precipitation and floods in the region of study. The discussion and concluding remarks are presented in Section 4.

2. Data and methods

a. Observational and reanalysis data

We use daily precipitation from the North American Regional Reanalysis (NARR) dataset (Mesinger et al. 2006) to characterize extreme cool season (November to March) precipitation events in the VRB and ARs during the period 1979/80-2010/11. Additionally, we analyze daily IWVT, 500-hPa geopotential height (HGT), 850-hPa wind, and low and high cloud cover fields from both NARR and the European Centre for Medium-Range Weather Forecasts (ECMWF) Interim Reanalysis (ERA-Interim) (Dee et al. 2011). In order to infer synoptic-scale vertical motion, we also (a) calculate **Q**-vectors and **Q**-vector convergence for the 700-400 hPa layer, and (b) examine pressure, specific humidity and system-relative winds at the 300-K isentropic surface derived from NARR data that were regridded to lower resolution to remove the noise in the calculations.

The NARR assimilation project is an extension of the National Centers for Environmental Prediction (NCEP) Global Reanalysis and provides data for North America and adjacent oceans. The NARR model uses the high resolution NCEP Eta

Model (32-km grid spacing) in conjunction with the Regional Data Assimilation System (RDAS) which assimilates precipitation from NCEP / Climate Prediction Center (CPC) along with other variables. On the other hand, ERA-Interim is the latest global atmospheric reanalysis produced by ECWMF and uses a coupled atmosphere-land-ocean forecast model with a horizontal spectral resolution of T255 (about 80 km) and 60 vertical model levels, with the model top at 0.1 hPa. Data from the SSM/I instruments are assimilated into this reanalysis system.

For the two extreme cases discussed in this work, we produce composite IWV fields using measurements from the SSM/I and SSMIS (SSM/I with sounding capabilities) instruments onboard the polar-orbiting Defense Meteorological Satellite Program (DMSP) F08, F10, F11, F13, F14, F15, F16 and F17 satellites. The SSMIS instruments operate in the latter two.

In addition, we use daily snow water equivalent (SWE) observations collected at three stations of the US Natural Resources Conservation Service SNOpack TELemetry (SNOTEL) network located within the VRB to evaluate the contribution of impacting ARs to the total snow accumulation in the basin for the water years (WYs) 1983-2011. We also examine daily-averaged streamflow data from the US Geological Survey (USGS) gauging sites for the period 1979-2011. The description of the SNOTEL and USGS stations is provided in Table 1 and the location of these measuring sites is presented in Figure 1.

b. Extreme precipitation events and AR detection

As a first step, we calculate daily area-average precipitation over the VRB. Using this time series, we then select the days that exceed the 98th percentile and define them as extreme events. The next step is to identify the subset of extreme precipitation events that are associated with AR occurrence. We use two criteria to objectively identify AR occurrence for each of the selected events based on the magnitude of the IWVT fields from ERA-Interim and NARR. The first criterion is an application of the algorithm developed by Zhu and Newell (1998) to classify the flux at each grid point along a given latitude either as AR flux or broad flux. An AR flux is defined as the flux whose magnitude ($\left|\mathrm{IWVT}\right|_{\mathrm{AR}}$) satisfies:

$$\left|\mathrm{IWVT}\right|_{\mathrm{AR}} \geq \left|\mathrm{IWVT}\right|_{\mathrm{mean}} + 0.3\left(\left|\mathrm{IWVT}\right|_{\mathrm{max}} - \left|\mathrm{IWVT}\right|_{\mathrm{mean}}\right),$$

where $\left|IWVT\right|_{mean}$ denotes the zonal mean of the magnitude of the IWVT along the corresponding latitude, and $\left|\mathrm{IWVT}\right|_{\mathrm{max}}$ is the magnitude of the maximum flux along that latitude. The constant 0.3 is an adjustable parameter chosen to appropriately represent the horizontal filamentary structure of the ARs. The second criterion uses a threshold of $\left|IWVT\right| \geq 250$ kg m^{-1} s^{-1} to detect the presence of vapor transport corridors with lengths of about 2000 km or longer (Ralph et al. 2012). For a given extreme precipitation day, an AR event is said to occur when both criteria are met using either of the two reanalysis datasets.

c. Statistical and composite analyses

The spatial patterns associated with ARs affecting the Southwest can be different from those that impact the West Coast of the US. To characterize the dominant spatial patterns we identify the principal modes of variability of the anomalous water vapor flux (AR "types") by performing a combined empirical orthogonal function (CEOF) analysis of the daily zonal and meridional IWVT anomalies for the days classified as "AR days". The IWVT anomalies are defined as departures from the 30-year daily climatological (November to March 1980/81-2009/10) values. The advantage of using CEOF is that it allows a simultaneous analysis of the modes of variability of multiple or vector-valued fields (Navarra and Simoncini 2010; Wilks 2011). We use the methodology of North et al. (1982) to assess the robustness of a given CEOF by calculating the 95% confidence error of the associated eigenvalue. A particular CEOF is statistically significant if the error bar does not overlap with the error bars of neighboring CEOFs.

To further characterize the atmospheric conditions associated with ARs that impacted the VRB, we perform a composite analysis of total IWVT, precipitation, 500-hPa HGT, 850-hPa winds, horizontal water vapor flux, **Q**-vector convergence, and cloud fraction fields for the days that are characteristic of each of the relevant modes identified in the CEOF analysis. To do this, we select the AR days in which the normalized principal component (PC) value exceeded one standard deviation.

3. Results

a. ARs and extreme precipitation events

Table 2 shows the list of the 97 extreme precipitation events. Based on our detection criteria, 57 of the events were associated with ARs. Most of the cool seasons listed have one or two AR events associated with extreme precipitation, but some of them present intense activity (three or more non-consecutive AR events) such as 1979/80, 1981/82, 1982/1983, 1992/93, and 2004/05. We find no clear relationship between the cool seasons of intense activity and El Niño - Southern Oscillation (ENSO) occurrence.

The extreme precipitation associated with ARs provided, on average, 25% of the total cool season precipitation in a few extreme events (the percentage ranges from 10% to 50%, depending on the season). In terms of snow accumulations, an analysis of the SNOTEL data, similar to that by Guan et al. (2010, 2012), for the three stations within the basin indicates that AR-related extreme events produced SWE gains of approximately 25-35% of the seasonal peak SWE accumulation (SWE_{max}). Such SWE percentages resemble those found by Guan et al. (2010, 2012) for the Sierra Nevada in California.

Extreme AR-related precipitation can also lead to flooding events in the VRB, depending on the precipitation phase and antecedent soil moisture conditions. For example, during the January and February 1993 AR events, the flow gages at both the lower Verde River below Tangle Creek and the upper Verde River near Clarkdale registered their largest daily discharge in the 1979-2011 record (January 8th and February 20th, respectively). Notably, in the lower part of the basin, the measured streamflow exceeded the 95th percentile in 28 out of 57 AR events. This is true for 24 out of 57 AR events on the upper VRB, and indicates that extreme discharge in the basin is largely associated with the occurrence of ARs.

b. CEOF analysis

We performed the CEOF analysis to identify some of the most important atmospheric conditions associated with the occurrence of the 57 AR episodes. The two dominant CEOF modes of NARR IWVT anomalies and their corresponding PCs are presented in

Figure 2. We also applied this statistical method on the ERA-Interim data and the results between the two reanalyses were consistent. Therefore, we only present information derived from the NARR regional assimilation product.

The first CEOF explains about 35% of the total variance. This particular mode of variability (Figure 2a) depicts a long area of strong eastward IWVT anomalies (above 300 kg m^{-1} s^{-1} at the core) extending from Hawaii across the Pacific Ocean. The figure clearly shows how the ARs penetrate inland, after crossing the Baja Peninsula, and impact not only the VRB but also other regions in the Southwestern US (Arizona, New Mexico, southern California, southeastern Nevada, southern Utah, western Colorado) and northwestern Mexico.

The above results suggest that the CEOF 1 of the IWVT anomalies is closely related to the characteristic long AR water vapor transport corridor that is known to impact portions of the US West Coast. We will refer to this pattern as Type 1 AR. The common name given to some AR events of this type is “pineapple express”, because sometimes they allow direct entrainment of water vapor from the tropics near Hawaii that can contribute to extreme precipitation over the continent (e.g., Bao et al. 2006; Ralph et al. 2011).

The second CEOF, which explains 17% of the total variance, shows northward IWVT anomalies associated with heavy precipitation in the VRB with magnitudes of about 100-150 kg m^{-1} s^{-1} over the Gulf of California and the Baja Peninsula (Figure 2b). The anomalous southwesterly transport of water vapor impacts most parts of Arizona, New Mexico, southern Utah and northern Mexico. This CEOF mode corresponds to ARs that bring moisture from the tropical eastern Pacific waters and will be referred to as Type 2

ARs. Figure 2b suggests these ARs are shorter than Type 1 ARs. Figure 2c presents the normalized PC time series for both Type 1 and Type 2 ARs. In this figure, the x-axis corresponds to the dates of ARs presented in Table 2. The dates that have a PC value larger than one are representative of each type of AR.

The corresponding eigenvalue spectrum for CEOFs 1 to 10 is depicted in Figure 2d. Using the North et al. (1982) rule, we find that both the first and second CEOF patterns are statistically significant at the 95% confidence level. As we will show in the following subsection, the two types of patterns seem to develop under distinct atmospheric conditions. However, it is important to note that because of the orthogonality constrain imposed in the CEOF analysis, we cannot state that there are only two fixed orientations of the impacting moisture flux bands. The data suggests that the dominant patterns are the end points of a range of possible directions.

Composite analysis

We generated a composite for those AR days in which the normalized PC values of each of the first two CEOF modes were greater than one standard deviation (see Table 2 and Figure 2c). In the days in which both PC values were above one standard deviation, we only considered the larger of the two. Table 2 lists the days used in the composite analysis for each mode. Figure 3a shows the composite IWVT field for Type 1 ARs. In this case, the column-integrated vapor flux into the VRB has a prominent zonal component over the low midlatitudes (as depicted by the first CEOF mode) and intensities that exceeded 300 kg m^{-1} s^{-1} in the core region off the west coast of the Baja Peninsula and 150-200 kg m^{-1} s^{-1} in several portions of Arizona. The composite precipitation patterns associated with this type of AR events are presented in Figure 3b. In central Arizona, the precipitation rate exceeds 20-30 mm day^{-1}, with maximum values above 40 mm day^{-1} in the eastern part of the VRB. Additionally, during the occurrence of Type 1 AR events, the largest precipitation intensities near the coast of southern California approximately range from 30 to 40 mm day^{-1}, and in the Sierra Nevada the rates are above 20 mm day^{-1}.

The cross section of horizontal water vapor flux along the NW-SE line offshore (L1 in Figure 3a) in Figure 3c shows greater transport below 850 hPa between 115°W and 120°W with a near surface maximum of 80 g kg^{-1} m s^{-1} at 118°W. The cross-section along the NW-SW line over land (Figure 3d, corresponding to line L2 in Figure 3a) shows that horizontal flux core values (> 60 g kg^{-1} m s^{-1}) are almost perpendicular to the topography and constrained to the lower levels above the surface across 106°W-114°W, i.e., Western Sierra Madre of Mexico, southern Arizona and the VRB region (111°W-114°W).

The composite 850-hPa winds and 500-hPa HGT in Figure 3e reveal a mid-level offshore trough, southwesterly low level winds of about 10 m s^{-1} crossing the Baja Peninsula and a ridge over the Gulf of Alaska. Additionally, over both Western US and the north Pacific there is a broad area of negative 500-hPa HGT anomalies (Figure 3f). This pattern resembles the anomalous atmospheric circulation conditions identified by Grotjahn and Faure (2008) for heavy precipitation in California and Ely et al. (1994) in their analysis of major winter floods in several basins in Arizona.

Figure 4a shows the composite IWVT for Type 2 ARs. Two of the most notable characteristics of these ARs are that they draw moisture directly from the tropical eastern Pacific and, as also indicated in the second CEOF mode of the IWVT anomalies, they are significantly shorter than Type 1 ARs. The core of the northward IWVT into the Southwestern US has values greater than 350-400 kg m^{-1} s^{-1} (similar to the IWVT intensity for Type 1 ARs). Over central Arizona, including the VRB, IWVT intensities are of about 200-250 kg m^{-1} s^{-1}.

The resulting composite precipitation for Type 2 ARs (Figure 4b) shows a similar spatial distribution as the first type of AR events. In Arizona, the largest precipitation rates (up to about 30-40 mm day^{-1}) occur in parts of the central highlands of Arizona, around the southern boundaries of the VRB. It is important to note that because of the mean orientation and position of the Type 2 ARs, the Sierra Nevada is not as strongly affected as in the case of Type 1 ARs. Hence, this particular region experiences lower precipitation rates.

The cross section along L1 (Figure 4c) indicates that the maximum horizontal vapor flux (about 80 g kg^{-1} m s^{-1}) is located at mid-levels of the troposphere (700 hPa) in the region between 112°W and 114°W. Additionally, the near surface flux has a major southerly component with intensities of 20-40 g kg^{-1} m s^{-1}. Cross-section L2 over land (Figure 4d), shows that the core horizontal water vapor flux is more intense and approximately located in the same geographical region as Type 1 ARs, but with a higher vertical extension. This may be due to the widespread vertical intrusion of water vapor from the oceanic source. Toward the VRB, the moisture flux reaches about 60 g kg^{-1} m s^{-1} at 750 hPa.

Figure 4e shows a 500-hPa trough off the US West Coast that penetrates into the subtropics. To the east of the trough there is a blocking ridge over the central US. Another ridge can be observed over the Gulf of Alaska. The same figure shows southerly 850-hPa flow into the Southwest. The position of the anomalous 500-hPa offshore low and the high pressure anomaly to the east favor the inland transport of tropical moist air from the eastern Pacific reservoir (Figure 4f).

Type 1 ARs also differ from Type 2 in the scale of the precipitation forming mechanisms. We use **Q**-vector convergence as a diagnostic tool to assess the impact of synoptic-scale processes on vertical motion (Lackmann, 2011). In Figure 5, the composites of **Q**-vector convergence in the 700-400 hPa layer show synoptic scale upward motion across the Southwestern US for both types of ARs. However, the convergence over Arizona for Type 1 ARs (Figure 5a) is less than that for Type 2 ARs (Figure 5b). Additionally, a close look at the composite low cloud cover for the former (Figure 5c) reveals that the higher fractions (above 80%-85%) are located along the state's central highlands, while relatively smaller fractions and more widespread low cloud cover distribution occur across the region in the latter (Figure 5d). In the case of high clouds, Figure 5e shows that for Type 1 ARs the covered fraction is smaller over the VRB and southern Arizona as compared to the coverage depicted in Figure 5f for Type 2 ARs. Smaller synoptic-scale forcing and predominance of low-level clouds suggest that both lifting and heavy rainfall during Type 1 ARs are strongly forced by orography at the mesoscale. On the other hand, precipitation during Type 2 ARs is not only affected by orographic forcing, but also shows stronger synoptic-scale forcing which results in a larger fraction of high-level clouds.

c. Selected AR cases

Below, we describe some of the most important hydrometeorological characteristics of two intense AR episodes that were responsible for major societal and economic impacts in the VRB and Arizona in general.

The first AR event occurred in 17 January 1993 (Case 1) and is related to a Type 1 AR that penetrated into the Southwestern US (PC1 > 1 > PC2). The episode was characterized by heavy precipitation in southern Arizona and parts of the central highlands, major flooding in the Santa Cruz River, and increase of snowpack (House and Hirschboeck 1997). As observed in the composite SSM/I IWV for the local morning of 17 January 1993 (Figure 6a), an AR is directed towards the west coast of the Baja Peninsula. The IWV core for this particularly strong AR exceeds 3 cm up to about 4 cm. The maximum IWVT intensities (Figure 6b) during the above day reached values greater than 450 kg m^{-1} s^{-1}, which are very similar to those reported for some strong ARs that have impacted California (e.g. Dettinger et al. 2011). The cross section along L1 (Figure 6c) shows a low level maximum in the horizontal water vapor flux field (80 g kg^{-1} m s^{-1}) between 116°W and 120°W (northern Baja Peninsula). In that same region, southwesterly horizontal transport, with intensities exceeding 60 g kg m^{-1} s^{-1}, dominates from surface up to about 600 hPa. Along L2, a maximum horizontal water vapor flux was directed toward the VRB (Figure 6d), therefore favoring the intensification of orographic precipitation in this area.

On the same day, a 500-hPa HGT gradient over the low midlatitudes in the north Pacific reveals the existence of a baroclinic zone. The associated westerly low-level jet showed maximum intensities of the order of 15 m s^{-1} at the 850-hPa level and the magnitude of winds off the northern Baja Peninsula was about 10 m s^{-1} (not shown). The 500-hPa HGT anomaly field (Figure 6e) presents a large region of anomalous low pressure over western US and the Pacific and an anomalous high pressure in the southern Baja Peninsula that favors the anomalous southwesterly flow (10-15 m s^{-1}) into the Southwest.

Extreme precipitation accumulations (30-50 mm) during Case 1 day were observed in the eastern VRB, as depicted in Figure 6f. The western portion of the basin received about 20-30 mm. The **Q**-vector convergence in Figure 6g shows very weak synoptic scale vertical motion over the basin and most parts of Arizona, which means that orographic forcing at the mesoscale is playing the dominant role on the generation of the extreme precipitation in the region, while the strongest upward motion is located mainly off the western coast of California. This is confirmed by isentropic analysis at the 300-K surface shown in Figure 6h (more intense system-relative upglide off the coast of California toward the low isentropic pressure and weak ascent of moist air over Arizona).

This AR episode also contributed to snow accumulations and high discharge in the region. During the period 16-18 January 1993, the White Horse Lake SNOTEL station registered positive SWE changes of about 69 mm. This represented 20% of the station's SWE_{max} for the WY 1993. Other two stations, Fry and Baker Butte, reported SWE increases of 51 mm (13% of SWE_{max}) and 46 mm (15% of SWE_{max}), respectively. On 17 January 1993, daily hydrological data for the period 1979-2011 show that the measuring site on the lower Verde River below Tangle Creek registered the third largest daily discharge for all Januaries (1022 m^3 s^{-1}). On the upper Verde River near Clarkdale, the streamflow reported on this particular day (368 m^3 s^{-1}) was the fourth largest for all Januaries.

The second event (Case 2) took place during 11 February 2005 and is classified as a Type 2 AR event (PC2 > 1 > PC1). During this period, excessive precipitation caused flooding as well as rock and mud slides in portions of Arizona (The Flood Control District of Maricopa County, http://www.fcd.maricopa.gov/education/history.aspx). Figure 7a shows a broad area of large IWV, with values of approximately 3-4 cm, directed towards the Southwest on the local evening of 11 February 2005. The IWVT field in Figure 7b for this particular day provides a clearer depiction of the impacting AR, with the south to north vertically integrated vapor flux exceeding 500 kg m^{-1} s^{-1}. In this case, it is evident that the moisture transported by this AR comes from the tropical reservoir in the eastern Pacific.

The horizontal water vapor flux along L1 (Figure 7c) has a maximum intensity of about 100 g kg^{-1} m s^{-1} off the coast of the southern part of the Baja Peninsula (112°W-114°W) between the vertical levels of 900 hPa and 800 hPa. Northward moisture transport exceeds 60 g kg^{-1} m s^{-1} from surface up to 450 hPa in the 110°W-114°W region. The cross section of moisture flux along L2 (Figure 7d), shows that the core of the vapor transport (> 80-100 g kg^{-1} m s^{-1}) spans from 108°W to 113°W. This means that the largest vapor flux is directed towards the VRB.

Intense northward low level anomalous winds of the order of 15 m s^{-1} into Arizona and a 500-hPa cut-off low over the Pacific to the west of the Baja Peninsula, with anomalies 100 m below climatology (Figure 7e) represent some the most significant weather patterns associated with this landfalling AR. Daily precipitation values above 50 mm due to this AR event were observed in the western vicinity of the VRB. The eastern portion of the basin did not receive as much precipitation (Figure 7f). This precipitation distribution is affected by the relatively strong synoptic scale upward motion to the west of the basin as depicted in the **Q**-vector convergence analysis (Figure 7g). In contrast to Case 1, this event shows stronger isentropic rising motion of moist air over central and northern Arizona (including the VRB region), southern California and the northern Baja Peninsula (Figure 7h).

During Case 2, the three SNOTEL stations located in the VRB reported SWE changes of less than 10% relative to the SWE_{max}. Based on the 32-year record used in this work, the USGS gage on the lower Verde River below Tangle Creek registered the fifth largest daily discharge for all Februaries (1140 m^3 s^{-1} on 12 February 2005). Similarly, on the upper Verde River near Clarkdale, the third largest daily streamflow value for all Februaries (500 m^3 s^{-1}) was measured on the same day.

In addition to the Type 1 and Type 2 ARs, a close inspection of the observations reveals AR events that are a mixture of both patterns. In particular, some days such as February 19th, 1993 and November 30th, 2007 have PC values larger than one for both modes. These cases can have IWVT patterns that are both zonal and meridional signatures, and they can also present double peaks in moisture transport at low-levels and mid-levels (not shown). This seems to indicate that the two "types" can be interpreted as end points of a range of possible directions.

4. Discussion and Conclusions

In this work we presented the first climatological characterization of AR events that affect the Southwestern US, with emphasis on Arizona, and discussed their role in generating extreme cool season (November to March) precipitation in the VRB for the period 1979/80-2010/11. We followed a "bottom-up" approach by first evaluating extreme daily precipitation in the VRB and selecting those extreme precipitation events that were associated with AR conditions. We then identified the dominant atmospheric patterns associated with these AR events by using a CEOF statistical tool.

Previous studies have developed different methodologies for AR identification. In our study, the criteria of Zhu and Newell (1998) and the criteria of Ralph et al. (2012) must be satisfied for a particular event to be labeled as AR. Using this method we identified 57 AR events. Notably, the extreme precipitation associated with ARs provided 25% of the total cool season precipitation in a few extreme events. Intense AR activity (three or more non-consecutive AR events) occurred during the cool seasons of 1979/80, 1981/82, 1982/1983, 1992/93, and 2004/05. However, we did not find a clear relationship between these active periods and ENSO. AR-related extreme events also produced SWE increases that represented 25-35% of the seasonal SWE_{max}. These SWE percentages are comparable to those estimated by Guan et al. (2010, 2012) for the Sierra Nevada in California. Additionally, almost half (49%) of the AR events were related to daily discharge above the 95th percentile of all daily values registered in the lower Verde River from 1979 to 2011.

Using CEOF analysis of zonal and meridional IWVT during the days of AR occurrence, we found two distinct "types" of ARs that affect the region. The first IWVT anomaly pattern represents west-to-east oriented ARs with core values above 300 kg m^{-1}

s^{-1} in the region between Hawaii and the west coast of the Baja Peninsula. The anomalous IWVT extends inland over the VRB and other regions in the Southwestern US. The cross section along the trajectory over the Pacific Ocean shows strong near surface horizontal vapor flux and as the AR penetrates inland, the core of the vapor transport (> 60 g kg^{-1} m s^{-1}) into the VRB (111°W-114°W) is concentrated in the lower levels above the surface. This mode resembles the long and narrow water vapor corridor associated with the landfalling ARs that have been analyzed in previous studies over the Western US, specifically in California (e.g., Ralph et al. 2004, 2005, 2006, Neiman et al. 2008, Dettinger et al. 2011, Ralph and Dettinger 2012), and we referred to it as Type 1 AR.

The interaction between the local topography and Type 1 ARs can lead to precipitation rates in the range of 20-50 mm day^{-1} across of the basin. Similarly, the coast of southern California and the Sierra Nevada receive 20-40 mm day^{-1} during the occurrence of these episodes. The extreme event in Arizona of 17 January 1993 is a specific example of Type 1 ARs. During this day, precipitation accumulations of 30-50 mm were observed in the eastern VRB. Additionally, the ARs of 20-22 January 2010, which we identified and characterized as Type 1 events (Table 2), were analyzed in depth by Neiman et al. (2013).

The second CEOF pattern describes a meridionally-oriented mode of anomalous water vapor transport into several parts of Arizona, New Mexico and southern Utah. We defined this pattern as Type 2 AR. These ARs are shorter than Type 1 ARs and draw moisture from the tropical reservoir in the eastern Pacific. The synoptic analysis of Type 2 ARs reveals the presence of a 500-hPa trough off the West Coast of the US that penetrates into lower latitudes. The cross section of horizontal vapor flux over the ocean shows core values at 700 hPa (i.e., at higher elevations than in Type 1 ARs). In addition, the composites indicate that both the intensities and spatial distribution of the precipitation are similar to those of Type 1 ARs, except for the lower rates in the Sierra Nevada. This is due to the meridional orientation of Type 2 ARs. The extreme precipitation episodes in Type 2 ARs seem to be associated with synoptic-scale vertical motion in addition to the orographic lifting mechanisms predominant in Type 1 ARs. A specific example of Type 2 AR occurred during 11 February 2005. A 500-hPa cut-off low off the coast of California and strong IWVT and low level winds from the tropical eastern Pacific characterized this event. Over the western vicinity of the VRB, the daily precipitation exceeded 50 mm while the eastern portion of the basin did not receive as much precipitation. The relationship between cut-off lows in the subtropical eastern Pacific that favor strong transport of tropical moisture into the Southwest and extreme precipitation events was previously examined by Knippertz and Martin (2007). Consistent with our results, their study finds that peak moisture transport during these events occurs at mid-levels, approximately 700 hPa, in contrast to the lower-level transport of midlatitude ARs. We also found dates of ARs events that have characteristic signatures of both Type 1 and Type 2 events.

It is very likely that nearby mountainous basins in the Southwestern US are affected by these water vapor corridors as well. One of the main characteristics of the impacting ARs is that they cross the Baja California Peninsula, which agrees with the findings of Rutz and Steenburgh (2012). Our study suggests that these Southwestern ARs do not form and develop in the same regions. While water vapor content in Type 1 ARs is obtained from the tropics near Hawaii (central Pacific) and enhanced in the midlatitudes, in Type 2 ARs moisture has a more direct tropical origin and meridional orientation.

Given the importance of the ARs in the distribution of cool season precipitation and extremes in the Southwestern US, it is important to understand their potential changes in intensity and frequency under a warmer climate. In previous work, Dettinger (2011) analyzed climate change projections under an A2 greenhouse-gas emissions scenario derived from seven general circulations models (GCMs) and found that the number of West Coast ARs with higher-than-average water vapor transport rates may increase and the length of the AR season would eventually extend in the future. Dominguez et al. (2012) analyzed an ensemble of regional climate models (RCMs) driven by IPCC AR4 GCMs under A2 emissions, and found a consistent and statistically significant increase in the intensity of future extreme winter precipitation events over the Southwestern US. While the statistical analysis was consistent among the models, the authors did not explore the physical mechanisms that were responsible for these changes. Because ARs may account for a large percentage of winter precipitation in many watersheds of the Southwestern US, we hypothesize that some of the increase in intensity of future extreme events projected by the RCMs may be due to changes in the intensity of the impacting ARs. This will be the focus of future studies.

Acknowledgements

Support for this study has been provided in part by the National Science Foundation (NSF) Grant 1038938. The work of Rivera was also partially supported by the Department of Energy (DOE) (DE-SC0001172) and the University of Costa Rica (UCR). Any opinions, findings, and conclusions or recommendations expressed in this publication are those of the authors and do not necessarily reflect the views of NSF, DOE or UCR. We would like to thank the three anonymous reviewers for their valuable comments and suggestions to improve this manuscript. NARR data are provided by the NOAA/OAR/ESRL PSD, Boulder, Colorado, USA, from their Web site at http://www.esrl.noaa.gov/psd/. SSM/I data are produced by Remote Sensing Systems and sponsored by the NASA Earth Science MEaSUREs DISCOVER Project. Data are available at http://www.remss.com. ECMWF ERA-Interim data used in this study have been obtained from the ECMWF Data Server (http://www.ecmwf.int).

References

Adams, D. K., and A. C. Comrie, 1997: The North American monsoon. *Bull. Amer. Meteor. Soc.*, **78**, 2197–2213.

Bao, J.-W., S. A. Michelson, P. J. Nieman, F. M. Ralph, and J. M. Wilczak, 2006: Interpretation of enhanced integrated water vapor bands associated with extratropical cyclones: Their formation and connection to tropical moisture. *Mon. Wea. Rev.*, **134**, 1063–1080.

Cavazos, T., and D. Rivas, 2004: Variability of extreme precipitation events in Tijuana, Mexico. *Climate Res.*, **25**, 229–243.

Dee, D. P., and Coauthors, 2011: The ERA-Interim reanalysis: Configuration and performance of the data assimilation system. *Quart. J. Roy. Meteor. Soc.*, **137**, 553–597.

Dettinger, M. D., 2011: Climate change, atmospheric rivers and floods in California – A multimodel analysis of storm frequency and magnitude changes. *J. Amer. Water Resources Assoc.*, **47**, 514–523.

Dettinger, M. D., F. M. Ralph, T. Das, P. J. Neiman, and D. Cayan, 2011: Atmospheric rivers, floods, and the water resources of California. *Water*, **3**, 455–478.

Dominguez, F., E. R. Rivera, C. L. Castro, and D. P. Lettenmaier, 2012: Changes in winter precipitation extremes for the western United States under a warmer climate as simulated by regional climate models. *Geophys. Res. Lett.*, **39**, L05803, doi:10.1029/2011GL050762.

Ely, L. L., Y. Enzel, and D. R. Cayan, 1994: Anomalous North Pacific atmospheric circulation and large winter floods in the southwestern United States. *J. Climate*, **7**, 977–987.

Grotjahn, R., and G. Faure, 2008: Composite predictor maps of extraordinary weather events in the Sacramento, California, region. *Wea. Forecasting*, **23**, 313–335.

Guan, B., N. P. Molotch, D. E. Waliser, E. J. Fetzer, and P. J. Neiman, 2010: Extreme snowfall events linked to atmospheric rivers and surface air temperature via satellite measurements. *Geophys. Res. Lett.*, **37**, L20401, doi:10.1029/2010GL044696.

Guan, B., D. E. Waliser, N. P. Molotch, E. J. Fetzer, and P. J. Neiman, 2012: Does the Madden–Julian oscillation influence wintertime atmospheric rivers and snowpack in the Sierra Nevada? *Mon. Wea. Rev.*, **140**, 325–342.

Hollinger, J. P., J. L. Peirce, and G. A. Poe, 1990: SSM/I instrument evaluation. *IEEE Trans. Geosci. Remote Sens.*, **28**, 781–790.

House, P. K., and K. K. Hirschboeck, 1997: Hydroclimatological and paleohydrological context of extreme winter flooding in Arizona, 1993. *Storm-Induced Geological Hazards: Case Histories from the 1992-1993 Winter Storm in Southern California and Arizona*. R. A. Larson, and J. E. Slosson, Eds., Geological Society of America Reviews in Engineering Geology, Boulder, Colorado, 1–24.

Knippertz, P., and J. E. Martin, 2007: A Pacific moisture conveyor belt and its relationship to a significant precipitation event in the semiarid southwestern United States. *Wea. Forecasting*, **22**, 125–144.

Lackmann, G. M., 2011: *Midlatitude Synoptic Meteorology: Dynamics, Analysis, and Forecasting*. American Meteorological Society, ISBN 978-1-878220-10-3, 345 pp.

Lavers, D. A., and G. Villarini, 2013: The nexus between atmospheric rivers and extreme precipitation across Europe. *Geophys. Res. Lett.*, **40**, 3259–3264, doi:10.1002/grl.50636.

Lavers, D. A., G. Villarini, R. P. Allan, E. F. Wood, and A. J. Wade, 2012: The detection of atmospheric rivers in atmospheric reanalyses and their links to British winter floods and the large-scale climatic circulation. *J. Geophys. Res.*, **117**, D20106, doi:10.1029/2012JD018027.

Leung, L. R., and Y. Qian, 2009: Atmospheric rivers induced heavy precipitation and flooding in the western U.S. simulated by the WRF regional climate model. *Geophys. Res. Lett.*, **36**, L03820, doi:10.1029/2008GL036445.

Mesinger, F., and Coauthors, 2006: North American regional reanalysis. *Bull. Amer. Meteor. Soc.*, **87**, 343–360.

Moore, B. J., P. J. Neiman, F. M. Ralph, and F. E. Barthold, 2012: Physical processes associated with heavy flooding rainfall in Nashville, Tennessee and vicinity during 1-2 May 2010: The role of an atmospheric river and mesoscale convective systems. *Mon. Wea. Rev.*, **140**, 358–378.

Navarra, A., and V. Simoncini, 2010: *A Guide to Empirical Orthogonal Functions for Climate Data Analysis*. 1st ed. Springer, 200 pp.

Neiman, P. J., F. M. Ralph, G. A. Wick, J. Lundquist, and M. D. Dettinger, 2008: Meteorological characteristics and overland precipitation impacts of atmospheric rivers affecting the west coast of North America based on eight years of SSM/I satellite observations. *J. Hydrometeor.*, **9**, 22–47.

Neiman, P. J., L. J. Schick, F. M. Ralph, M. Hughes, and G. A. Wick, 2011: Flooding in western Washington: The connection to atmospheric rivers. *J. Hydrometeor.*, **12**, 1337–1358.

Neiman, P. J., F. M. Ralph, B. J. Moore, M. Hughes, K. Mahoney, J. M. Cordeira, and M. D. Dettinger, 2013: The landfall and inland penetration of a flood-producing atmospheric river in Arizona. Part 1: Observed synoptic-scale, orographic, and hydrometeorological characteristics. *J. Hydrometeor.*, **14**, 460–484.

North, G. R., T. L. Bell, R. F. Cahalan, and F. J. Moeng, 1982: Sampling errors in the estimation of empirical orthogonal functions. *Mon. Wea. Rev.*, **110**, 699–706.

Ralph, F.M., and M. D. Dettinger, 2011: Storms, floods and the science of atmospheric rivers. *EOS, Transactions, Amer. Geophys. Union*, **92**, 265–266.

Ralph, F. M., and M. D. Dettinger, 2012: Historical and national perspectives on extreme West Coast precipitation associated with atmospheric rivers during December 2010. *Bull. Amer. Meteor. Soc.*, **93**, 783–790.

Ralph, F. M., P. J. Neiman, and G. A. Wick, 2004: Satellite and CALJET aircraft observations of atmospheric rivers over the eastern North Pacific Ocean during the winter of 1997/98. *Mon. Wea. Rev.*,**132**, 1721–1745.

Ralph, F. M., P. J. Neiman, and R. Rotunno, 2005: Dropsonde observations in low-level jets over the northeastern Pacific Ocean from CALJET-1998 and PACJET-2001:

Mean vertical-profile and atmospheric-river characteristics. *Mon. Wea. Rev.*, **133**, 889–910.

Ralph, F. M., P. J. Neiman, G. A. Wick, S. I. Gutman, M. D. Dettinger, D. R. Cayan, and A. B. White, 2006: Flooding on California's Russian River: Role of atmospheric rivers. *Geophys. Res. Lett.*, **33**, L13801, doi:10.1029/2006GL026689.

Ralph, F. M., P. J. Neiman, G. N. Kiladis, K. Weickmann, and D. W. Reynolds , 2011: A multi-scale observational case study of a Pacific atmospheric river exhibiting tropical-extratropical connections and a mesoscale frontal wave. *Mon. Wea. Rev.*, **139**, 1169–1189, doi: 10.1175/2010MWR3596.1.

Ralph, F. M., G. A. Wick, P. J. Neiman, B. J. Moore, J. R. Spackman, M. Hughes, F. Yong, and T. Hock, 2012: Atmospheric rivers in reanalysis products: A six-event comparison with aircraft observations of water vapor transport. *WCRP Reanalysis Conference, Washington, DC, USA.*

Redmond, K. T., and R. W. Koch, 1991: Surface climate and streamflow variability in the western United States and their relationship to large scale circulation indices. *Water Resour. Res.*, **27**, 2381–2399.

Roberge, A., J. R. Gyakum, E. H. Atallah, 2009: Analysis of intense poleward water vapor transports into high latitudes of western North America. *Wea. Forecasting*, **24**, 1732–1747.

Rutz, J. J., and W. J. Steenburgh, 2012: Quantifying the role of atmospheric rivers in the interior western United States. *Atmos. Sci. Let.*, **13**, 257–261.

Sheppard, P. R., A. C. Comrie, G. D. Packin, K. Angersbach, and M. K. Hughes, 2002: The climate of the US Southwest. *Climate Res.*, **21**, 219–238.

Smith, B. L., S. E. Yuter, P. J. Neiman, and D. E. Kingsmill, 2010: Water vapor fluxes and orographic precipitation over northern California associated with a land-falling atmospheric river. *Mon. Wea. Rev.*, **138**, 74–100.

Sodemann, H., and A. Stohl, 2013: Moisture origin and meridional transport in atmospheric rivers and their association with multiple cyclones. *Mon. Wea. Rev.*, **141**, 2850–2868.

Stohl, A., C. Forster, and H. Sodemann, 2008: Remote sources of water vapor forming precipitation on the Norwegian west coast at 60° N - A tale of hurricanes and an atmospheric river. *J. Geophys. Res.*, **113**, D05102, doi:10.1029/2007JD009006.

U.S. Army Corps of Engineers, 1994: *Flood damage report, State of Arizona, floods of 1993*. U.S. Army Corps of Engineers, Los Angeles District, 107 pp.

Viale, M., and M. N. Nuñez, 2011: Climatology of winter orographic precipitation over the subtropical central Andes and associated synoptic and regional characteristics. *J. Hydrometeor.*, **12**, 481–507.

Wick, G. A., P. J. Neiman, and F. M. Ralph, 2013: Description and validation of an automated objective technique for identification and characterization of the integrated water vapor signature of atmospheric rivers. *IEEE Trans. Geosci. Remote Sensing*, **51**, 2166–2176.

Wilks, D. S., 2011: *Statistical Methods in the Atmospheric Sciences*. 3rd Edition, Academic Press, Amsterdam, 676 pp.

Zhu, Y., and R. E. Newell, 1998: A proposed algorithm for moisture fluxes from atmospheric rivers. *Mon. Wea. Rev.*, **126**, 725–735.

Table 1. Description of the SNOTEL and USGS stations used in this study. (See Figure 1 for location of the sites.)

Dataset	Variable	Station name	Latitude (°N)	Longitude (°W)	Elevation (m)
SNOTEL	Daily SWE (mm)	Baker Butte	34.45	111.40	2225
		Fry	35.07	111.83	2195
		White Horse Lake	35.13	112.13	2190
USGS	Daily discharge (m^3 s^{-1})	Tangle Creek	34.07	111.72	618
		Clarkdale	34.85	112.07	1067

Table 2. Cool season (November to March) extreme events in the VRB during 1979/80 – 2010/11 based on area-averaged extreme daily precipitation accumulations (pcp; units of mm) exceeding the 98th percentile. Dates (event numbers) in bold indicate the occurrence of AR days (events). An asterisk (*) denotes days used in the Type 1 AR composites. A pound sign (#) denotes days used in the Type 2 AR composites.

Event	Year	Month	Day	pcp (mm)	Event	Year	Month	Day	pcp (mm)	Event	Year	Month	Day	pcp (mm)
1	**1980**	**01**	**10***	**27.7**	34	1990	02	19	22.9	**67**	**1998**	**03**	**26**	**18.5**
2	**1980**	**01**	**29***	**35.2**	**35**	**1991**	**01**	**04**	**23.7**	68	2001	12	04	19.9
3	**1980**	**02**	**14***	**41.6**	**36**	**1991**	**02**	**28***	**47.3**	**69**	**2003**	**02**	**13***	**41.7**
4	**1980**	**02**	**15***	**20.3**	**37**	**1991**	**03**	**01***	**45.6**	70	2003	02	26	18.7
5	**1980**	**02**	**20***	**31.8**	38	1991	11	15	19.5	**71**	**2003**	**03**	**16**	**15.5**
6	**1981**	**02**	**09***	**17.5**	39	1991	11	30	15.6	**72**	**2003**	**11**	**12**$^{\#}$	**21.0**
7	1981	03	02	20.0	40	1992	01	06	23.7	**73**	**2003**	**11**	**13**	**18.8**
8	**1981**	**11**	**27**$^{\#}$	**17.5**	**41**	**1992**	**02**	**13***	**24.5**	74	2004	11	08	22.4
9	**1981**	**11**	**28**$^{\#}$	**18.7**	42	1992	03	08	17.1	75	2004	11	21	21.5
10	1981	11	29	20.5	**43**	**1992**	**12**	**04**	**33.2**	**76**	**2004**	**12**	**29***	**50.7**
11	1982	01	21	20.6	**44**	**1992**	**12**	**28**$^{\#}$	**35.0**	**77**	**2005**	**01**	**04***	**35.7**
12	**1982**	**02**	**11***	**24.7**	**45**	**1993**	**01**	**06***	**23.2**	**78**	**2005**	**02**	**11**$^{\#}$	**16.2**
13	**1982**	**03**	**12**	**15.8**	**46**	**1993**	**01**	**07***	**28.9**	79	2005	02	12	35.8
14	1982	11	09	23.0	**47**	**1993**	**01**	**08***	**25.4**	80	2005	02	19	16.6
15	**1982**	**11**	**30**	**31.7**	**48**	**1993**	**01**	**17***	**28.2**	81	2007	03	23	16.1
16	**1982**	**12**	**09**	**16.3**	**49**	**1993**	**01**	**18**	**16.7**	**82**	**2007**	**11**	**30**$^{\#}$	**18.9**
17	1983	01	28	19.7	50	1993	01	30	15.5	**83**	**2007**	**12**	**01***	**42.1**
18	**1983**	**02**	**03**$^{\#}$	**18.0**	**51**	**1993**	**02**	**08***	**35.2**	84	2008	01	07	25.8
19	**1983**	**03**	**03***	**24.7**	52	1993	02	09	20.9	**85**	**2008**	**01**	**27**$^{\#}$	**29.3**
20	**1983**	**12**	**25***	**20.2**	**53**	**1993**	**02**	**19***	**19.7**	86	2008	02	04	17.3
21	1984	11	23	20.4	**54**	**1993**	**02**	**20**	**18.6**	87	2008	11	27	18.9
22	1984	12	13	21.4	55	1993	03	27	19.2	**88**	**2008**	**12**	**17**$^{\#}$	**15.5**
23	**1984**	**12**	**27**$^{\#}$	**36.0**	**56**	**1994**	**02**	**08**	**25.2**	89	2008	12	26	16.3
24	**1985**	**11**	**12***	**28.5**	57	1994	12	06	15.7	90	2009	12	08	17.4
25	**1985**	**11**	**25***	**28.5**	**58**	**1995**	**01**	**05**	**28.4**	**91**	**2010**	**01**	**20***	**18.1**
26	1985	11	26	18.5	59	1995	01	26	19.8	**92**	**2010**	**01**	**21***	**54.3**
27	1986	12	06	21.5	**60**	**1995**	**02**	**14***	**23.3**	**93**	**2010**	**01**	**22***	**37.9**
28	1987	02	24	27.6	**61**	**1995**	**02**	**15***	**18.0**	94	2010	02	07	16.5
29	**1987**	**11**	**01***	**36.0**	62	1995	03	06	19.4	95	2010	03	07	17.3

30	**1988**	**01**	**18**	**32.7**	63	1997	01	13	35.0	96	2010	12	23	21.1
31	**1989**	**01**	**04#**	**33.2**	**64**	**1997**	**01**	**26**	**17.5**	**97**	**2011**	**02**	**19**	**21.5**
32	**1989**	**03**	**26**	**27.6**	65	1997	02	28	18.3					
33	1989	12	29	21.7	66	1997	12	22	17.8					

Figure captions

Figure 1. Topographical map of the Southwestern US. The Verde River Basin in Arizona is delineated in black. Triangles denote the SNOTEL stations: Baker Butte (black), Fry (white), and White Horse Lake (gray). Circles denote the USGS stations: Verde River below Tangle Creek (black), and Verde River near Clarkdale (white). (See Table 1 for description of the measuring sites.)

Figure 2. Spatial pattern of the IWVT anomalies (kg m^{-1} s^{-1}; gray shadings with vectors superimposed) for (a) CEOF 1, and (b) CEOF 2. (c) Normalized principal component (PC) time series of CEOFs 1 and 2 where the x axis corresponds to the dates of events presented in Table 2. The horizontal line denotes the one standard deviation and is used to determine those AR days in which the normalized PC exceeds one standard deviation. (d) Eigenvalue spectrum of the first ten CEOFs of the IWVT field.

Figure 3. Composite (a) IWVT (kg m^{-1} s^{-1}; gray shadings with vectors superimposed), (b) precipitation (mm day^{-1}), (c) – (d) cross section of horizontal water vapor flux (g kg^{-1} m s^{-1}; contours with vectors superimposed) along L1 and L2, respectively, (e) total fields and (f) anomalies of 500-hPa HGT (m; contours) and 850-hPa winds (barbs = 10 m s^{-1}, half barbs = 5 m s^{-1}) for the selected Type 1 ARs (see Table 2). The NW-SE lines, L1 and L2, in panel (a) are the lines for the cross sections in panels (c) and (d), respectively.

Figure 4. Same as Figure 3 but for Type 2 ARs.

Figure 5. Composite (a) – (b) **Q**-vectors (×10^{-10} K m^{-1} s^{-1}) and 2×**Q**-vector convergence (×10^{-16} K m^{-2} s^{-1}; contours; gray shadings for convergence or upward motion) for the 700-

400 hPa layer, (c) – (d) low cloud fraction (%), and (e) – (f) high cloud fraction (%) for Type 1 and Type 2 ARs, respectively.

Figure 6. (a) SSM/I IWV (cm), (b) IWVT (kg m^{-1} s^{-1}; gray shadings with vectors superimposed), (c) – (d) cross section of horizontal water vapor flux (g kg^{-1} m s^{-1}; contours with vectors superimposed) along L1 and L2, respectively, (e) anomalies of 500-hPa HGT (m; contours) and 850-hPa winds (barbs = 10 m s^{-1}, half barbs = 5 m s^{-1}), (f) accumulated precipitation (mm), (g) **Q**-vectors ($\times 10^{-10}$ K m^{-1} s^{-1}) and 2×**Q**-vector convergence ($\times 10^{-16}$ K m^{-2} s^{-1}; contours; gray shadings for convergence or upward motion) for the 700-400 hPa layer, and (h) pressure (hPa; contours), system-relative winds (barbs = 10 m s^{-1}, half barbs = 5 m s^{-1}) and specific humidity (g kg^{-1}; gray shadings) on the 300-K isentropic surface for 17 January 1993. The NW-SE lines, L1 and L2, in panel (b) are the lines for the cross sections in panels (c) and (d), respectively.

Figure 7. Same as Figure 6 but for 11 February 2005.

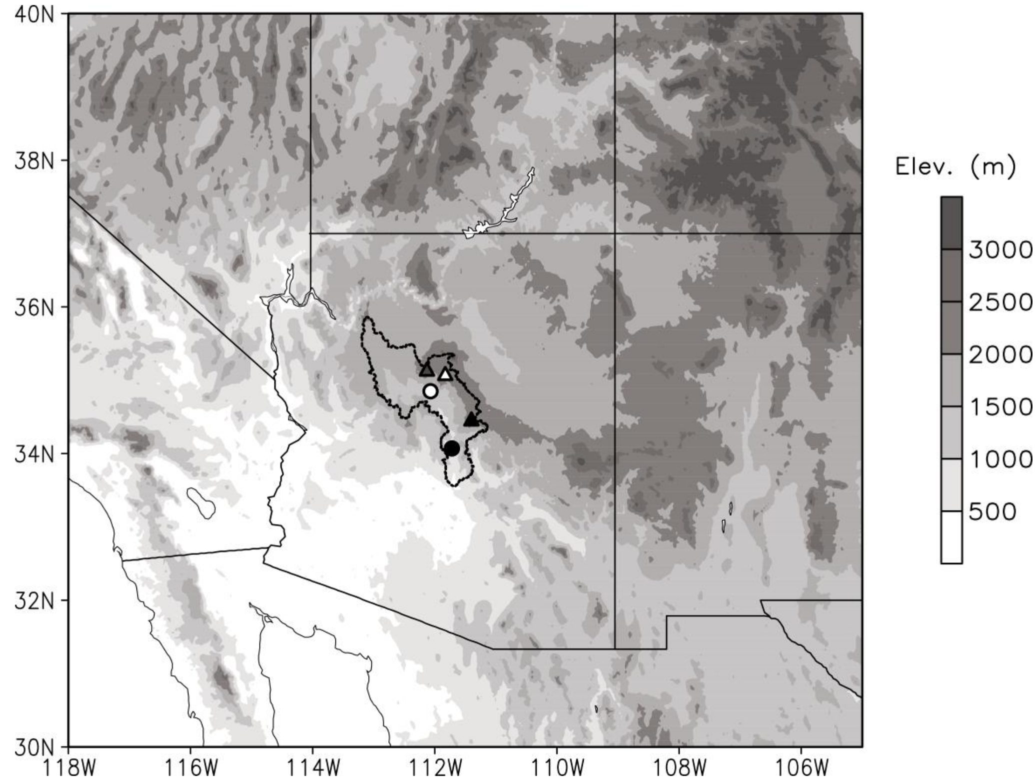

Figure 1. Topographical map of the Southwestern US. The Verde River Basin in Arizona is delineated in black. Triangles denote the SNOTEL stations: Baker Butte (black), Fry (white), and White Horse Lake (gray). Circles denote the USGS stations: Verde River below Tangle Creek (black), and Verde River near Clarkdale (white). (See Table 1 for description of the measuring sites.)

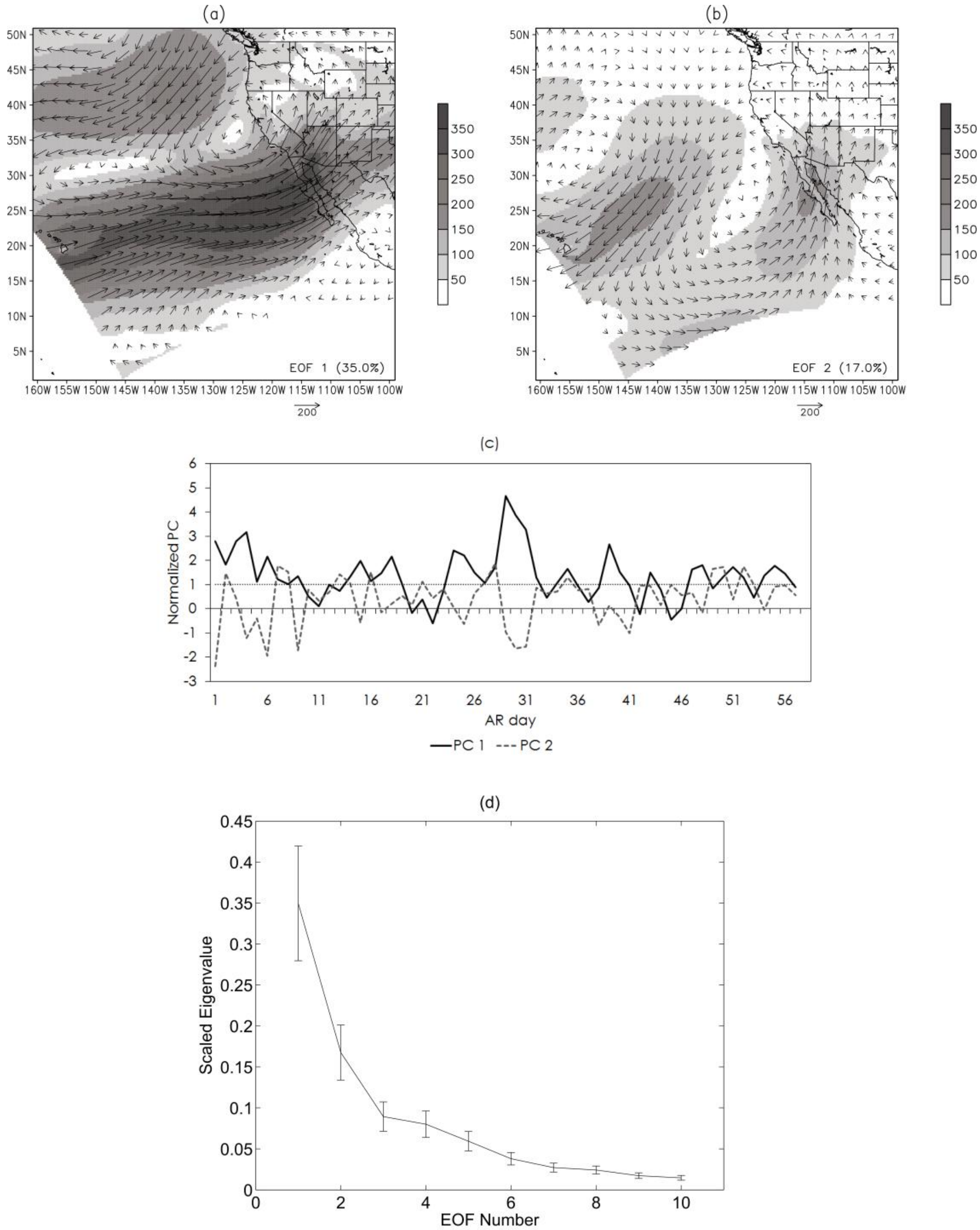

Figure 2. Spatial pattern of the IWVT anomalies (kg m^{-1} s^{-1}; gray shadings with vectors superimposed) for (a) CEOF 1, and (b) CEOF 2. (c) Normalized principal component (PC) time series of CEOFs 1 and 2 where the x axis corresponds to the dates of events presented in Table 2. The horizontal line denotes the one standard deviation and is used to determine those AR days in which the normalized PC exceeds one standard deviation. (d) Eigenvalue spectrum of the first ten CEOFs of the IWVT field.

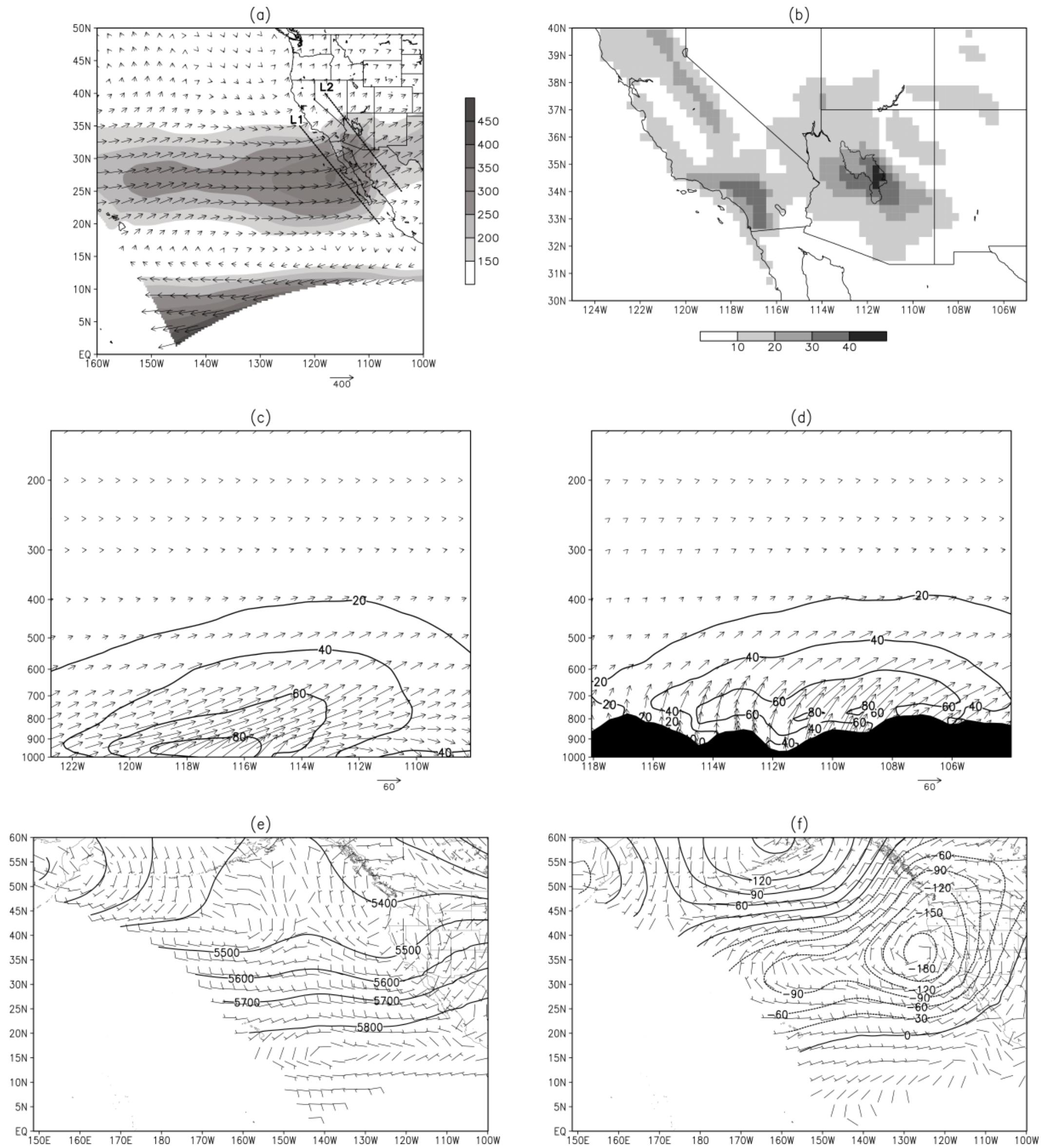

Figure 3. Composite (a) IWVT (kg m^{-1} s^{-1}; gray shadings with vectors superimposed), (b) precipitation (mm day^{-1}), (c) – (d) cross section of horizontal water vapor flux (g kg^{-1} m s^{-1}; contours with vectors superimposed) along L1 and L2, respectively, (e) total fields and (f) anomalies of 500-hPa HGT (m; contours) and 850-hPa winds (barbs = 10 m s^{-1}, half barbs = 5 m s^{-1}) for the selected Type 1 ARs (see Table 2). The NW-SE lines, L1 and L2, in panel (a) are the lines for the cross sections in panels (c) and (d), respectively.

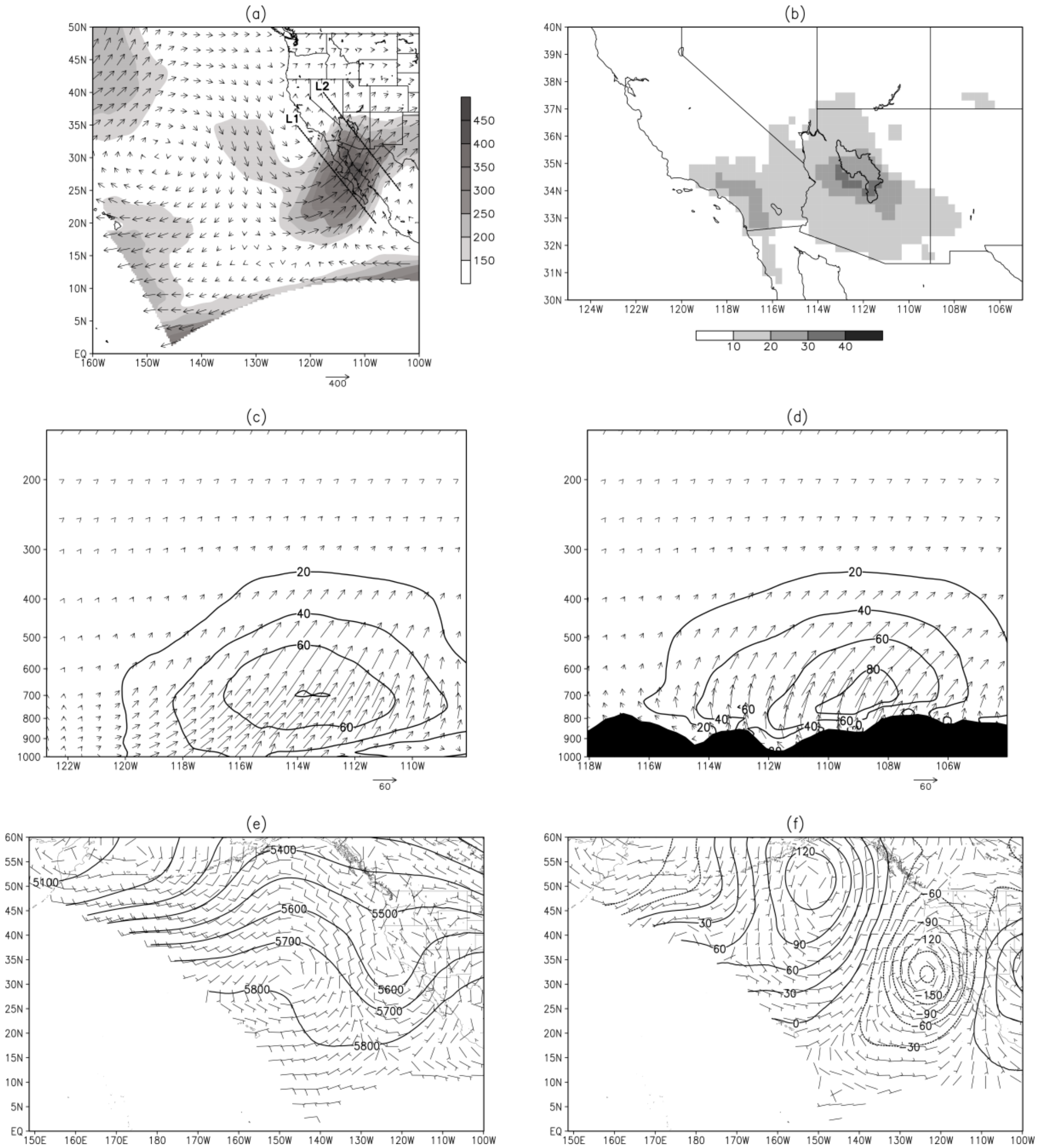

Figure 4. Same as Figure 3 but for Type 2 ARs.

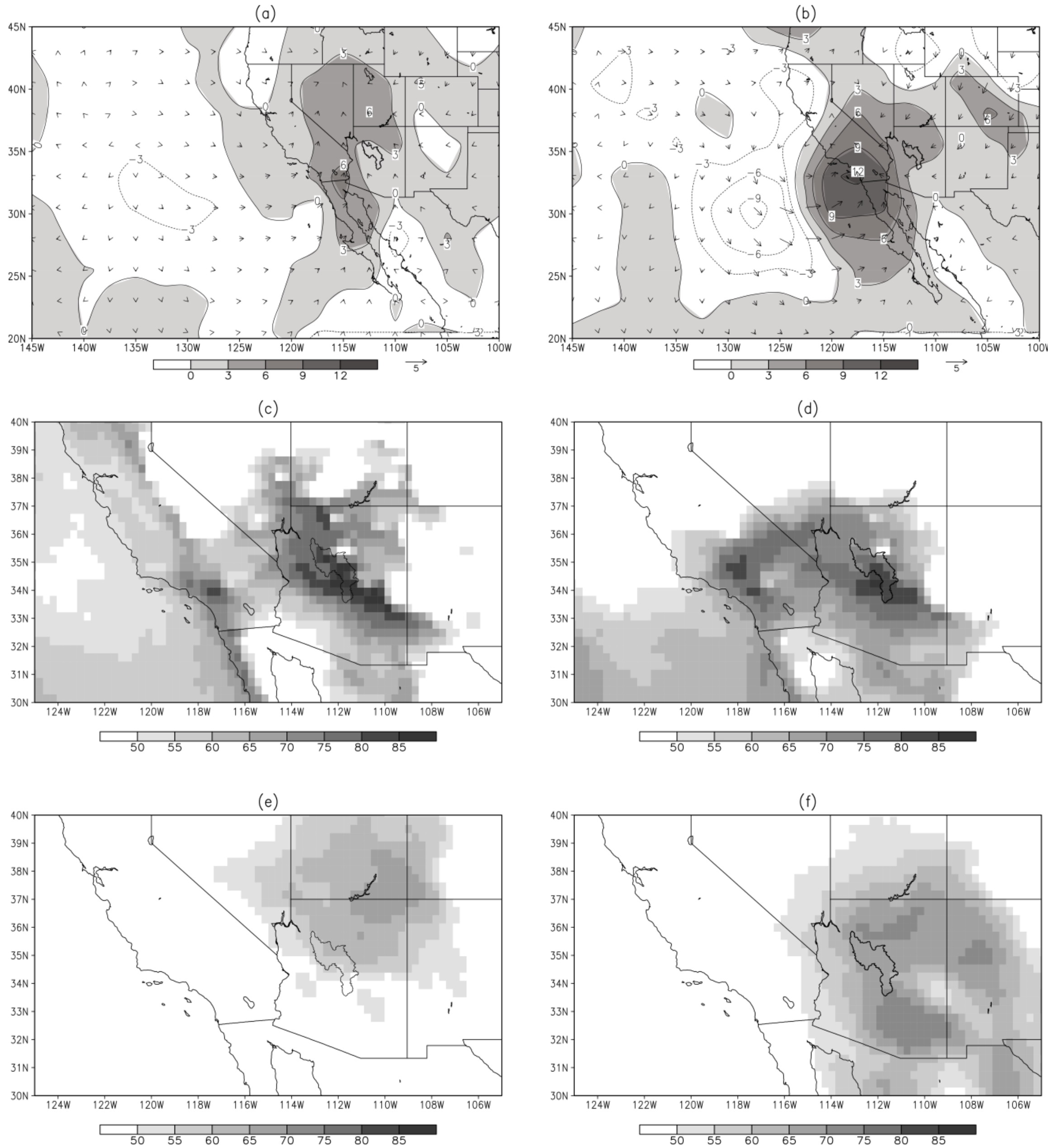

Figure 5. Composite (a) – (b) **Q**-vectors ($\times10^{-10}$ K m^{-1} s^{-1}) and 2×**Q**-vector convergence ($\times10^{-16}$ K m^{-2} s^{-1}; contours; gray shadings for convergence or upward motion) for the 700-400 hPa layer, (c) – (d) low cloud fraction (%), and (e) – (f) high cloud fraction (%) for Type 1 and Type 2 ARs, respectively.

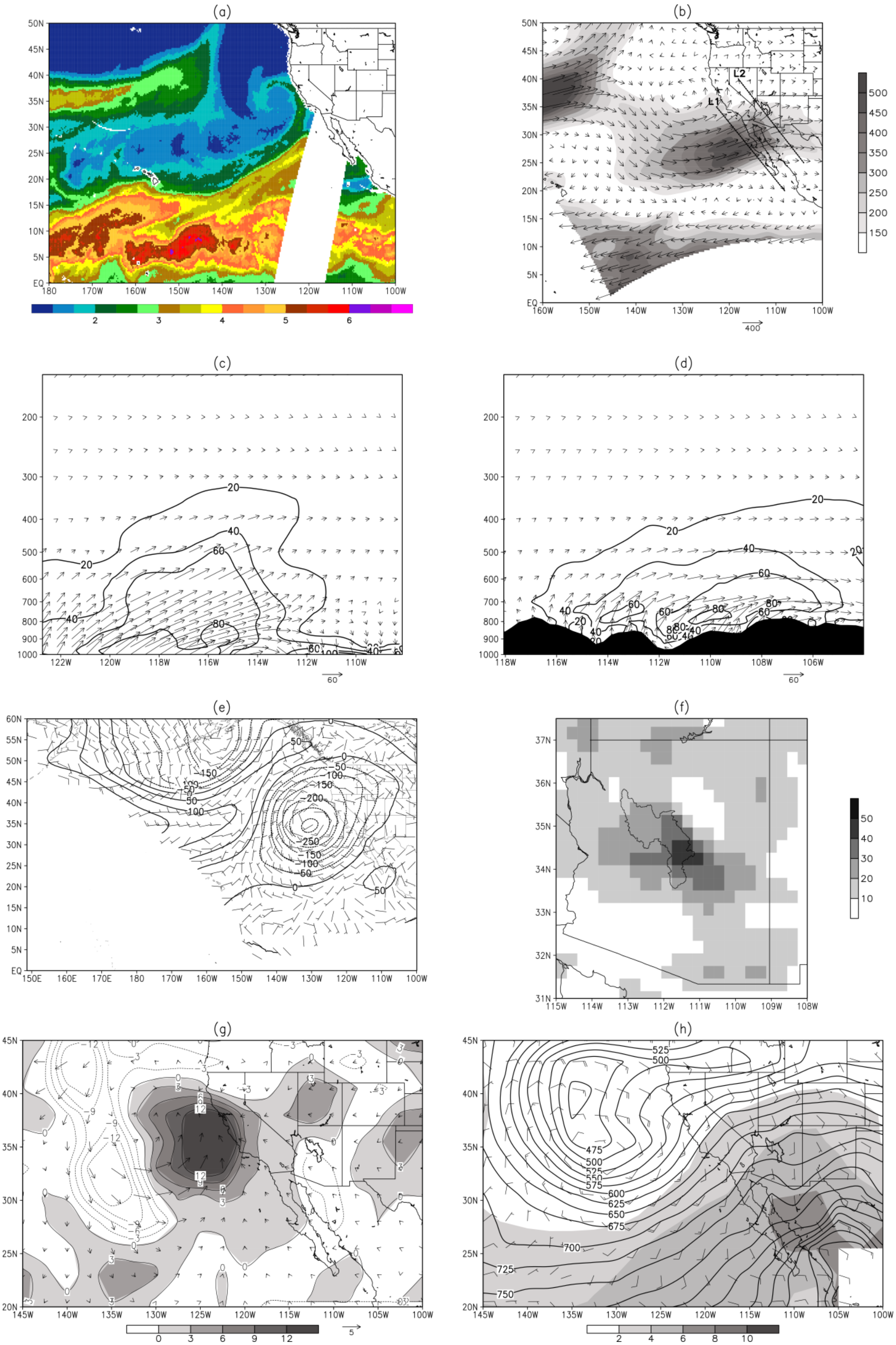
(a)
(b)
L1
L2
(c)
(d)
(e)
(f)
(g)
(h)

Figure 6. (a) SSM/I IWV (cm), (b) IWVT (kg m^{-1} s^{-1}; gray shadings with vectors superimposed), (c) – (d) cross section of horizontal water vapor flux (g kg^{-1} m s^{-1}; contours with vectors superimposed) along L1 and L2, respectively, (e) anomalies of 500-hPa HGT (m; contours) and 850-hPa winds (barbs = 10 m s^{-1}, half barbs = 5 m s^{-1}), (f) accumulated precipitation (mm), (g) **Q**-vectors ($\times10^{-10}$ K m^{-1} s^{-1}) and 2×**Q**-vector convergence ($\times10^{-16}$ K m^{-2} s^{-1}; contours; gray shadings for convergence or upward motion) for the 700-400 hPa layer, and (h) pressure (hPa; contours), system-relative winds (barbs = 10 m s^{-1}, half barbs = 5 m s^{-1}) and specific humidity (g kg^{-1}; gray shadings) on the 300-K isentropic surface for 17 January 1993. The NW-SE lines, L1 and L2, in panel (b) are the lines for the cross sections in panels (c) and (d), respectively.

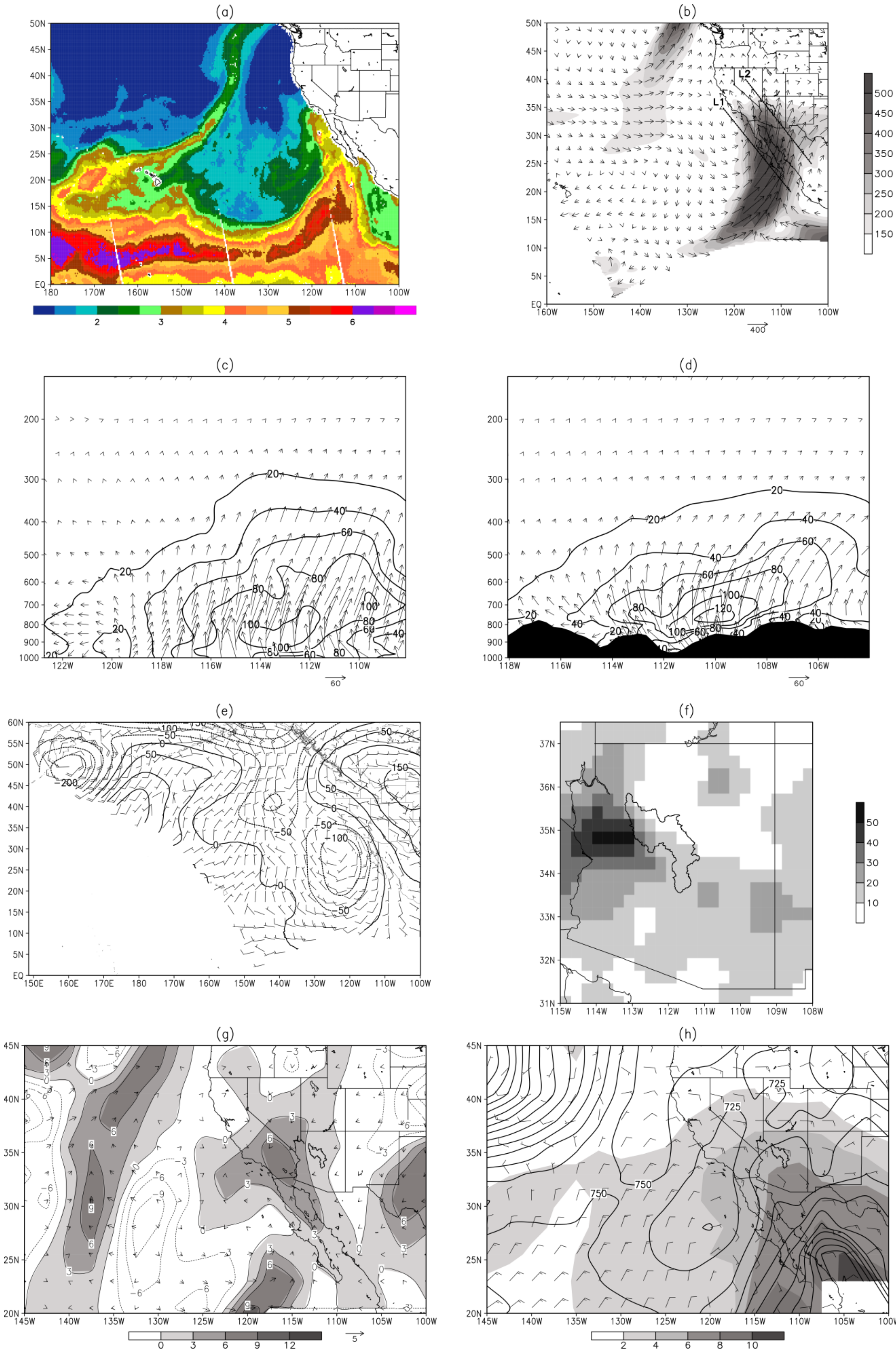
(a)
(b)
L1
L2
(c)
(d)
(e)
(f)
(g)
(h)

Figure 7. Same as Figure 6 but for 11 February 2005.